ELSEVIER

In situ AFM study of the dissolution and recrystallization behaviour of polished and stressed calcite surfaces

J. Bisschop [a,*], D.K. Dysthe [a], C.V. Putnis [b], B. Jamtveit [a]

[a] *Physics of Geological Processes, University of Oslo, PO Box 1048 Blindern, 0316 Oslo, Norway*
[b] *Institut für Mineralogie, Universität Münster, Corrensstrasse 24, D-48149 Münster, Germany*

Abstract

We investigated the dissolution behaviour of polished calcite surfaces in situ using a fluid-cell atomic force microscope. Polished calcite surfaces enabled us to study the effects of applied surface stress and crystallographic orientation on calcite dissolution pattern formation. Thin-sections of Iceland spar single-crystals polished either parallel or with a 5° miscut angle to $\{10\bar{1}4\}$ cleavage planes were studied. Compressive surface stresses of up to 50 MPa were applied to some of the thin-section samples by means of elastic concave bending. Experiments were carried out in semi-stagnant deionized water under mainly transport limited dissolution conditions. Samples polished parallel to $\{10\bar{1}4\}$ cleavage planes dissolved by the formation of etch-pits originating from polishing defects. The dissolution behaviour of 5° miscut surfaces was relatively unaffected by polishing defects, since no etch-pits developed in these samples. Dissolution of the miscut samples led to stepped or rippled surface patterns on the nanometer scale that coarsened during the first 30–40 min of the experiments. Possible reasons for the pattern-coarsening were: (i) progressive bunching of retreating dissolution steps and (ii) surface energy driven recrystallization (Ostwald ripening) under transport limited dissolution conditions. A flat polished miscut surface in calcite may recrystallize into a hill-and-valley structure in a (near-)saturated solution so as to lower its total surface free energy in spite of a larger surface area. No clear effect of applied stress on dissolution pattern formation has been observed.
© 2006 Elsevier Inc. All rights reserved.

1. Introduction

The dissolution and precipitation behaviour of calcite has been widely studied since it plays an important role in rock-weathering, soil chemistry, and biomineralization processes. Moreover, calcite is an abundant rock-forming mineral in the earth's upper crust, and at depth, dissolution and precipitation of calcite underlie processes such as pressure solution compaction, stylolite formation, and crack-healing in calcite-bearing sediments or rocks. Much knowledge about the nano- to micrometer scale mechanisms of calcite dissolution and precipitation has been acquired by means of fluid-cell atomic force microscopy (e.g., Liang and Baer, 1997; Lea et al., 2001; Teng, 2004). Traditionally, these studies are carried out on the calcite $\{10\bar{1}4\}$ cleavage

surface since AFM imaging requires flat surfaces and calcite dissolves layer-by-layer along these crystallographic planes. In this paper, we report fluid-cell AFM experiments carried out on *polished* calcite surfaces. Polished sample surfaces enabled us to study the effect of applied stress and crystallographic orientation on the dissolution behaviour of calcite.

In order to understand how aqueous fluids interact with calcite-bearing rocks loaded by overburden or tectonic stresses, it is important to know how much stress affects the dissolution mechanisms and rates of calcite. Applied stress increases the potential (elastic strain) energy of crystals and hence their solubility in aqueous solutions (Paterson, 1973). A significant increase in dissolution rate of ionic crystals upon the application of stress has been reported for, e.g., calcite (Gutman, 1994) and sodium chlorate (Morel and Den Brok, 2001). An understanding of the effect of crystallographic orientation on the dissolution

* Corresponding author. Fax: +47 22 85 51 01.
E-mail address: Jan.Bisschop@fys.uio.no (J. Bisschop).

mechanisms and rates of calcite is important, since natural calcite surfaces such as grain boundaries and fracture surfaces are expected not to be parallel to $\{10\bar{1}4\}$ cleavage surfaces in general. The higher the miscut angle of a surface with the $\{10\bar{1}4\}$ cleavage planes, the higher the number of elementary steps on the calcite dissolution front and the higher the reaction site density and surface energy are to be expected (e.g., Venables, 2000). In calcite-saturated brines, elastic strain energy and surface energy may drive recrystallization of calcite through a dissolution–precipitation mechanism. Normal stress induced recrystallization of rocks/minerals in a saturated solution is known as 'pressure solution' and is an important mechanism of compaction of (calcite-bearing) sedimentary rocks (e.g., Spiers et al., 2004). Surface energy induced recrystallization of particles, i.e., Ostwald ripening, is an important process during diagenesis and prograde metamorphism of calcite-bearing sediments/rocks (Chai, 1974; Morse and Casey, 1988).

In the case of stress applied parallel to a dissolution front, elastic strain energy and surface energy are competing driving forces of pattern formation on crystal surfaces in a (near-) saturated solution. On the one hand, stress tends to roughen crystal surfaces since dissolution preferably occurs from surface depressions where stress-concentrations exist. Surface energy, on the other hand, may drive a minimization of surface roughness through a dissolution–precipitation mechanism. This competition may lead to a surface morphology with a characteristic wavelength (Srolovitz, 1989; Misbah et al., 2004) and explains the observations of grooves or ripples on stressed crystal surfaces in aqueous solutions (Den Brok and Morel, 2001; Koehn et al., 2004). This stress-induced surface instability is known as the so-called Grinfeld instability. In this paper we investigated the effect of applied surface-parallel stress on the initial evolution of dissolution patterns in calcite using a fluid-cell AFM. The effect of stress was studied in samples polished parallel or with a 5° miscut to the $\{10\bar{1}4\}$ cleavage planes, i.e., for calcite surfaces with a low or high density of elementary steps, respectively.

2. Method

2.1. Material and sample preparation

We have studied the dissolution behaviour of 15 calcite single-crystal samples (7 stress-free; 8 stressed) in situ using AFM. All samples were prepared from four large cleavage rhomb crystals of Iceland Spar from Chihuahua, Mexico (Ward's Natural Science). The source crystals were of high optical quality, i.e., free of fluid and solid inclusions and cleavage cracks as seen by the naked eye. Trace element chemistry of the four crystals (C1, C2, C3, and C4) was measured with an Atom Scan 25 ICP Emission Spectrometer (Table 1). The sample surface was ground on successively finer grinding paper and finished with 1 μm diamond paste suspension followed by Struers OP-U

Table 1
Trace element chemistry of four source crystals analyzed with ICP emission spectrometry

Element	C1	C2	C3	C4
Mg	4317[a]	4035	4842	6456
Mn	196	161	411	107
Sr	336	392	157	224

[a] Parts per million $CaCO_3$; concentrations Ti, Zn, V, Cr, Cu, and Ce below detection limit.

(0.04 μm colloidal silica suspension), resulting in a final roughness (root mean square) of around 1 nm. Polishing led to calcite surfaces with low and equal roughness, but polishing also caused surface defects altering the dissolution behaviour of the material.

We developed a new method to elastically strain calcite crystals under the AFM: thin-sections of the crystals were prepared and subsequently bent to apply a compressive surface stress. Thin-sections of calcite are very brittle and break upon the slightest bending along cleavage planes. To avoid this from happening, the calcite thin-sections with a thickness of 60–80 μm were prepared on microscope cover glasses with a thickness of 200 μm. Upon bending of this double-layer the neutral plane of bending (i.e., the plane of zero strain) lies within the glass piece and as a result the complete calcite slice is under compressive stress and does not break. In order to make a thin-section on a cover glass, the cover glass was glued with a very thin layer of wax onto a 1-mm thick microscope glass. After thin-section preparation the cover glass with the calcite slice was detached from the microscope glass by warming the wax. The thin-sections were glued into polished concave Perspex holders with constant curvatures in the range of 15–25 cm (Fig. 1). Stress-free samples were thin-sections glued onto flat holders or thick polished sections.
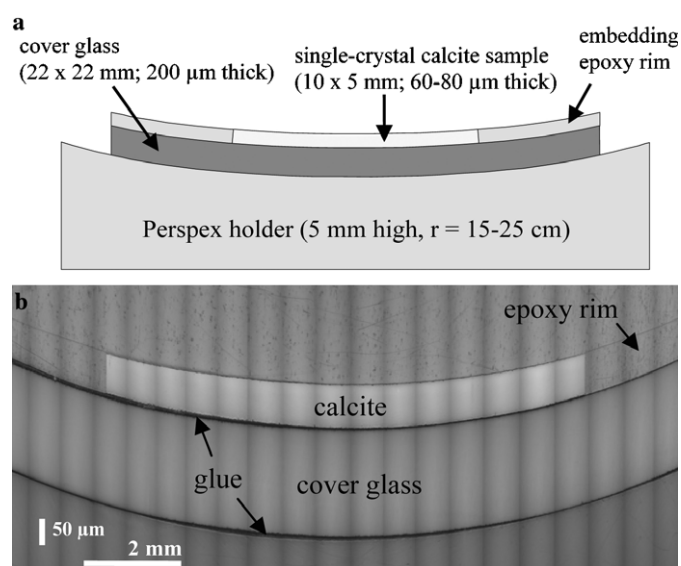

Fig. 1. Type of elastically strained samples studied in this project. (a) Schematic cross-section view of thin-section sample glued into a concave Perspex holder. (b) Stretched image of a cross-section of sample S5 (curvature radius of 230 mm).

The principal stress direction in our experiments is the $\langle 40\bar{4}1 \rangle$-direction, the intersection line of two cleavage planes (Fig. 2). This stress orientation is highly unfavorable for the initiation of mechanical twins (De Bresser and Spiers, 1997). Twins were avoided in our experiments since they may affect the dissolution behaviour (Engelder, 1982). The $[40\bar{4}1]$ and $[0\bar{4}41]$ directions (in a hexagonal unit cell), commonly labeled as the $[48\bar{1}]$ and $[\bar{4}41]$ directions, are referred to as the *A*- and *B*-direction, respectively, in this paper. Samples were either polished parallel or with a 5° miscut angle to a $\{10\bar{1}4\}$ cleavage planes to obtain sample surface with low or a high initial density of elementary surface steps. Compressive surface stresses given in Table 2 are calculated analytically on basis of measured sample thicknesses and curvatures. The position of the neutral surface in the double-layer sample upon bending was calculated using the equation for bending of an elastically isotropic plate (e.g., Watts, 2001). We assumed perfect stick between the two layers (calcite and glass) and no net-shortening of the sample upon bending. The calculated surface stresses need to be considered as approximate since calcite is elastically anisotropic. In the calculation we used an approximate Young's modulus of 57 GPa for calcite in the $[0\bar{4}41]$-direction and a corresponding Poisson's ratio of 0.39. The Young's Modulus of the cover glass is 72.9 GPa and the Poisson's ratio 0.208 (manufacturer's specification).

2.2. AFM experiments

In this project, a Veeco (Digital Instruments) Dimension 3000 AFM with a fluid tip holder was used. A Teflon fluid-chamber holder was built that fitted our curved thin-section assemblage of $23 \times 23 \times 7$ mm. Water flow through the cell was controlled manually by pumping water in and out using two syringes. Just before (ca. 30 min) an experiment the thin-section was freshly polished with 0.04 μm colloidal silica suspension, cleaned for a few seconds with distilled water, and quickly dried. Subsequently, the thin-section was glued onto a curved or flat holder and the whole assemblage was thoroughly cleaned with alcohol such that it would not contaminate the water in the fluid-cell. The polished crystal surface was cleaned briefly with alcohol using a soft tissue. AFM-images were taken randomly over the 5×10 mm sample surface, but away from the sample edges. In the case of stressed samples the scan line direction was perpendicular to the fold-axis of the sample curvature. When using holders with the largest curvature ($r = 15$ cm), the thin-section assemblage needed to be slightly tilted such that the rear end of the tip holder did not touch the sample surface.

All experiments were carried out in purified deionized water (Milli-Q, 18.2 MΩ cm) at room temperature. The deionized water was prepared freshly on a daily basis and poured into a large syringe and pumped into the open

Table 2
Overview of experiments

Spl.	S^a	Miscut angle (°)	t^b (min)	Sample thickness	Stress (MPa)
SF1	C1	0	118	~2 mm	0
SF2	C1	~1	125	~2 mm	0
SF3	C2	5	134	79 μm	0
SF4	C2	5	134	77 μm	0
SF5	C3	5	209	~2 mm	0
SF6	C3	5.3	156	90 μm	0
SF7	C3	5.3	88	~2 mm	0
S1	C1	0	66	72 μm	40
S2	C1	0	156	78 μm	36
S3	C3	5.5	179	73 μm	46
S4	C3	5	116	70 μm	46
S5	C3	5	179	82 μm	31
S6	C3	5.5	189	72 μm	45
S7	C4	5	127	57 μm	48
S8	C4	5	135	74 μm	44

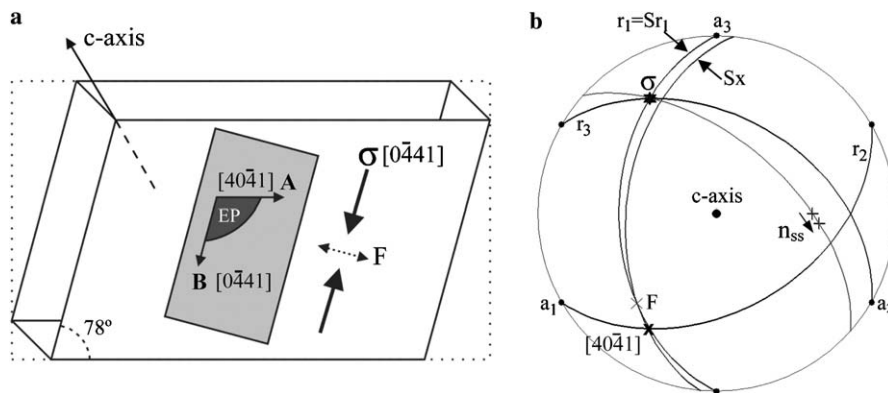[a] Source crystals given in Table 1.
[b] Duration of experiment.

Fig. 2. Crystallographic orientation of samples. (a) Outline of rhombic calcite crystal indicating the position of the thin-section of 5×10 mm in the $\{10\bar{1}4\}$ cleavage plane. EP is the outline of an etch-pit with a rounded corner (cf. Lea et al., 2001) and etch-pit walls with crystallographic directions *A* and *B*. Thin-sections are stressed by bending around a fold axis F, resulting in a principal stress direction σ $[0\bar{4}41]$. (b) Stereonet projection (equal area; upper hemisphere) showing crystallographic axes *C*, a_1, a_2, and a_3; three cleavage plane sets r_1, r_2, and r_3; axis of sample curvature (F); and principal stress direction σ for non-miscut samples. Samples surfaces are either parallel (S_{r1}) or inclined by the 5° (S_x) to $\{10\bar{1}4\}$ cleavage planes. The inclined sample surface is obtained by a 5° rotation of the sample surface normal (n_{ss}) away from the *c*-axis on a great-circle with pole *F* (as shown by arrow). As a result the principal stress direction also rotates by 5°.

fluid-cell. The water in the fluid-cell was refreshed after every first or second image taken, every 5 or 10 min. Thus, during image acquisition the fluid flow was stopped and apart from water movement induced by the AFM-tip scanning, the condition of the water was stagnant. The initial pH of the inlet water is assumed to be in between 5.5 and 6, a typical pH of a small volume of freshly prepared deionized water briefly exposed to air. We did not monitor the changes of ion concentrations in the fluid and therefore the dissolution rate in our experiments is not known. As discussed in Section 4.1 dissolution in cleavage-parallel samples was initially probably surface reaction controlled, while in 5° miscut samples the high flux of atoms leaving the surface probably made dissolution rapidly transport controlled in the stagnant fluid. Calculations showed that, with a water layer thickness of 3–4 mm on top of the sample, CO_2-diffusion from the atmosphere to the reacting surface is likely to be the rate limiting step of dissolution during image acquisition, and that the bulk fluid did not become saturated with respect to CO_2 or Ca^{2+} in a time span of 5–15 min.

2.3. AFM image acquisition and analysis

A relatively low scan rate of 1.2 or 2 Hz was used to obtain high quality AFM images. For images of 512×512 pixels, these scan rates corresponded to acquisition times of 7 and 4 min, respectively. The time-gradient in Figs. 3, 4, 6a–f, and 11b is from top to bottom and in Figs. 6g and h, 10a–c, and 11a, from right to left. Data points in Figs. 5, 7, 9, and 12 are plotted at the time half of the image was acquired. Images were acquired in contact mode using silicon nitride probes (NP-S) with a tip radius curvature of 20–60 nm (manufacturer's specification). Although the force on the tip during scanning was reduced as much as possible, the tip-effect became increasingly significant upon repeated scanning of the same spot, especially on surfaces with growth features. For this reason most images were taken at different sample locations.

Roughness (RMS) and surface area were measured from AFM height mode images. In order to measure step-related surface morphology only, the global tilt and bow in the images were removed by a second-order flattening algorithm. Surface area (Fig. 9) is given as the percentage increase of the 3D surface area over the 2D surface area: $(A_{3D}/A_{2D} - 1) \times 100\%$. A_{3D} is the sum of the area of all of the triangles formed by three adjacent data points (pixels). The pattern-coarseness plotted in Fig. 7 is measured by counting all features edges (dark and bright lines) cross-cutting three parallel transects (3 or 5 μm long) perpendicular to the *A*-direction. The average step-spacing or ripple width is simply the transects length divided by the number of intersections. For a selected number of images we measured the step/ripple size distributions (Fig. 8) and these show the deviation of the average values plotted in Fig. 7.

3. Observations

3.1. Surfaces (sub)parallel to cleavage planes

Samples SF1 and SF2 polished (sub)parallel to $\{10\bar{1}4\}$ cleavage planes dissolved by etch-pit formation in deionized water (Fig. 3). The high initial number of etch-pits and the tendency of etch-pits to align (in polishing scratches) indicate that dissolution originated from polishing defects rather than from bulk lattice defects. Bulk dislocation densities reported for unstrained single-crystal calcite are, for instance, $\sim 10^6 \, cm^{-2}$ for annealed Iceland Spar (De Bresser, 1996) and less than $10^6 \, cm^{-2}$ for Shtall calcite (MacInnis and Brantley, 1992). The etch-pit densities in Figs. 3a and d correspond to 8.3×10^8 and $1.0 \times 10^9 \, cm^{-2}$, respectively, and thus are three orders of magnitude larger than bulk dislocation densities of unstrained calcite crystals. Polishing defects from which the etch-pits originated in our samples were likely dislocations (loops) and not pits or cracks. The etch-pits became much deeper than the polishing scratches they tend to align in, indicating that etch-pits were not simply a result of dissolution steps retreating from pre-existing polishing pits. Etch-pits initially had a conical-like shape and this indicates they grew from a 'line' source and not from 'surface' source (i.e., cracks). In sample SF2 dissolution after 99 min occurred dominantly along parallel steps while most etch-pits disappeared. The difference in the evolution of the dissolution patterns of samples SF1 and SF2 was probably a result of the actual misorientation of the sample surface with the $\{10\bar{1}4\}$ cleavage planes. In sample SF2 polishing resulted in a misorientation of 0.9° (Fig. 3f) and thus this surface contained a much higher initial density of elementary steps to start with.

Stressed samples S1 and S2 polished parallel to $\{10\bar{1}4\}$ planes dissolved by etch-pit formation (Fig. 4). Again, the initial high density ($\sim 10^9 \, cm^{-2}$) and alignment of etch-pits (in scratches) show that these etch-pits originated from defects caused by polishing. No effect of stress on etch-pit formation was observed. In all stress-free and stressed samples etch-pits initially had rhombohedral shape and during on-going dissolution the corners formed by the obtuse etch-pit walls became gradually more rounded (cf. Lea et al., 2001). The roughness evolution (root mean square) of stressed and stress-free samples during etch-pit formation was similar (Fig. 5). Up to 1 h into the experiments the roughness in the four samples increased more or less linearly with time and was not clearly affected by the applied stress. In sample SF2, the roughness did not increase after 1 hour, because etch-pits disappeared. In samples SF1 and S2, the roughness development also slowed down (or even decreased) after 80 and 60 min into the experiments, respectively. This was a result of etch-pits not becoming deeper and coalesence of adjacent etch-pit walls.
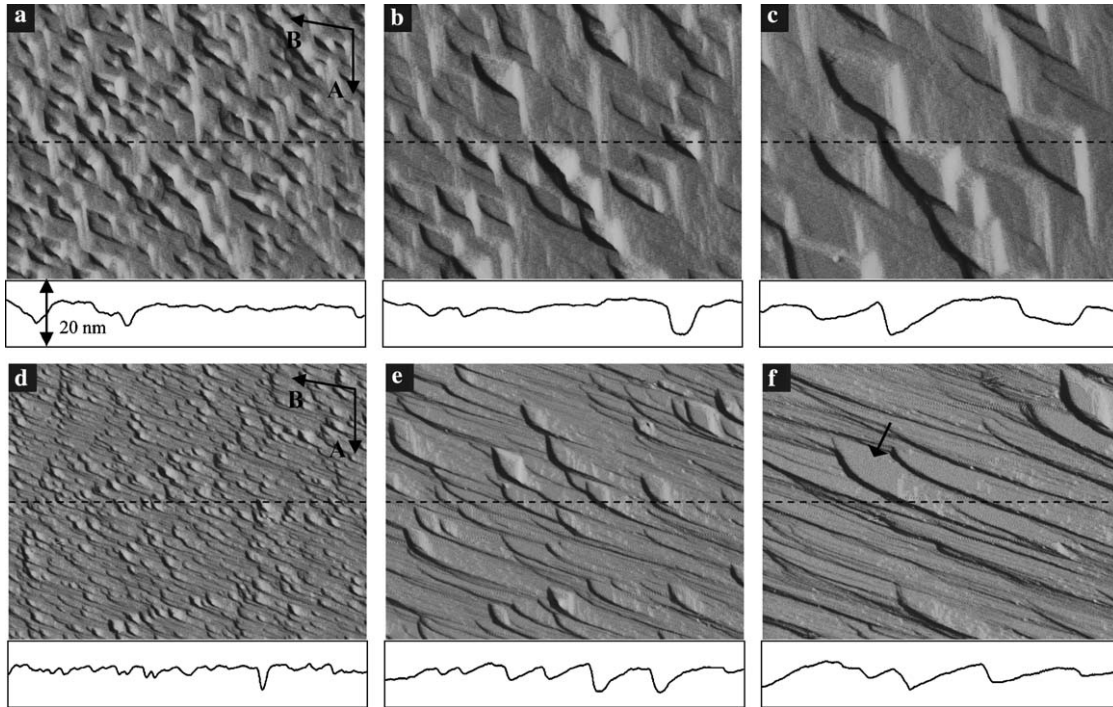
Fig. 3. In situ AFM (deflection) images of dissolution patterns in stress-free samples polished (sub) parallel to cleavage planes. Width of all images is 5 μm. The height profile curves are given for the dashed line in the AFM images. Height axis is 20 nm in all profile images. (a–c) Sample SF1—all images of the same location: (a) after 18 min (∼160 etch pits); (b) after 57 min (∼40 etch pits); (c) after 109 min (∼15 etch pits). (d–f) Sample SF2—all images of the same location: (d) after 23 min (∼200 etch pits); (e) after 61 min (∼20 etch pits); (f) after 99 min (3 etch pits). Arrow in (f) indicates a terrace at 0.9° to the sample surface.
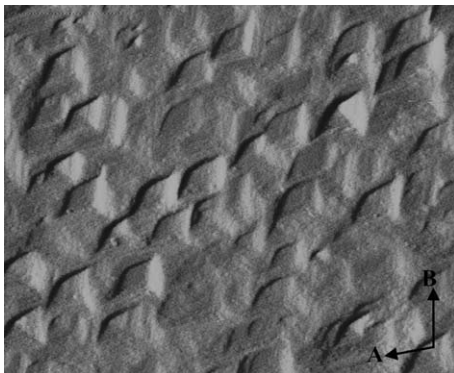
Fig. 4. In situ AFM (deflection) image of sample S1 after 61 min (∼70 etch-pits). Principal stress is 40 MPa in the B-direction. Image width is 5 μm.
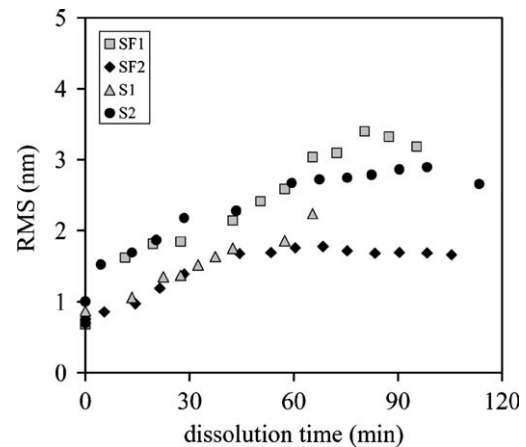

Fig. 5. Roughness (root mean square) development in samples with etch-pit formation. All images from same locations in the four experiments. RMS measured after second order flattening of the AFM height images.

3.2. Surfaces at 5° to cleavage planes

We studied 5 stress-free and 6 stressed calcite samples polished with a miscut angle of 5° to the $\{10\bar{1}4\}$ cleavage planes (Table 2). In none of the stress-free and stressed samples was the formation of etch-pits observed upon the addition of deionized water, while it is to be expected that these samples contain as many surface defects caused by polishing as do the cleavage-parallel samples. The aspect ratio of etch-pits in samples polished parallel to cleavage planes shows that widening was faster than deepening of etch-pits and that initial etch-pit walls generally made an

angle of less than 5° with cleavage planes (Figs. 3a and d). For this geometrical reason no etch-pits formed on the 5° miscut surfaces.

In stress-free sample SF3 the addition of water led to the formation of narrowly spaced dissolution steps (Fig. 6b). The steps were parallel to the A-direction, which is the expected preferred orientation of dissolution steps for the given miscut direction. The dissolution steps cross-cut the dense streaking of polishing scratches visible on the dry surface (Fig. 6a) suggesting that polishing defects do
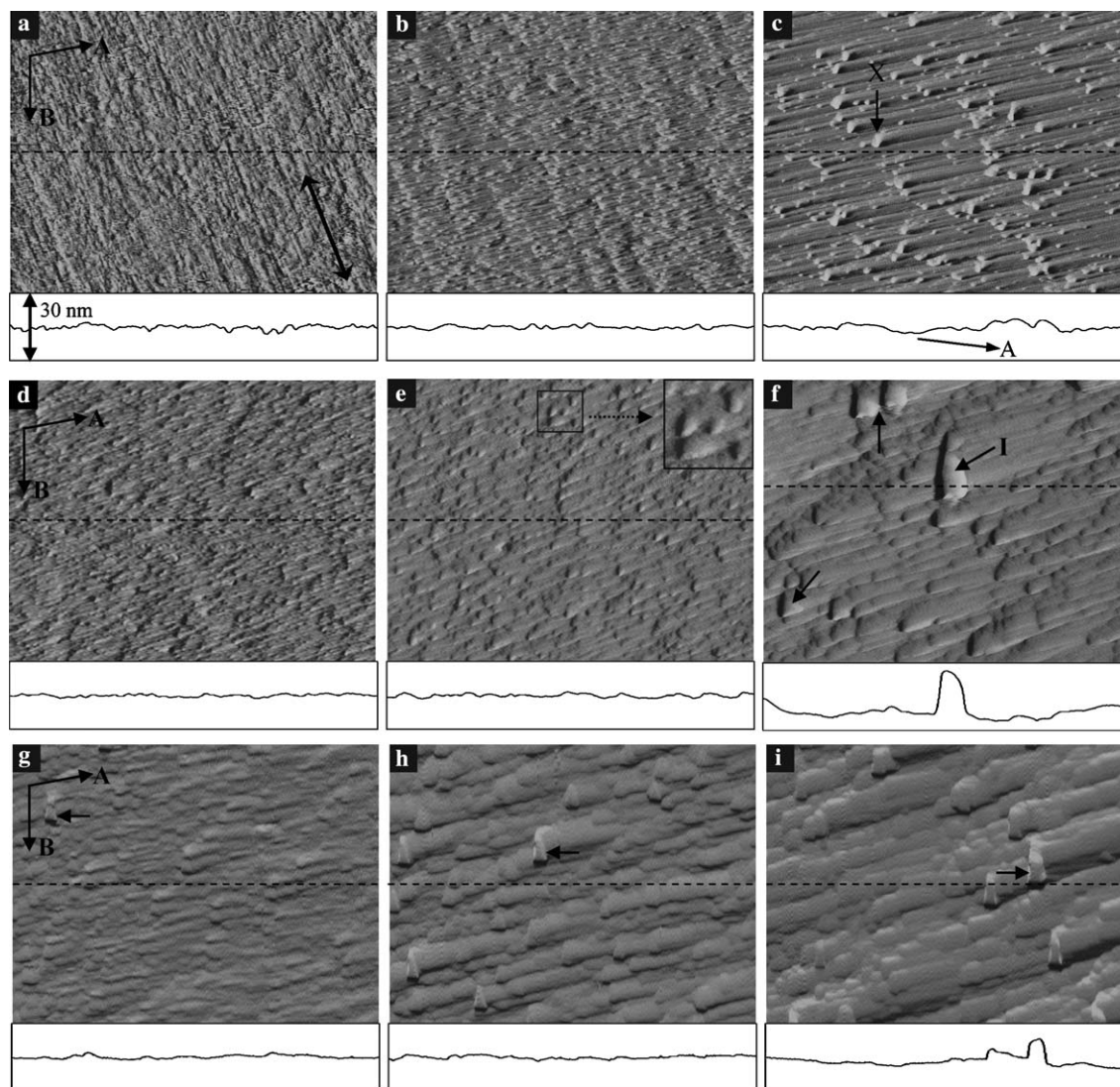
Fig. 6. In situ AFM (deflection) images of samples with a 5° miscut; all images taken at different spots (with exception of a and b). The height profile curves are given for the dashed line in the AFM images. Height axis is 30 nm in all profile images. (a–c) Sample SF3; width of images is 5 μm: (a) initial dry surface; arrow parallel to polishing scratches; (b) after 5 min, same spot as (a); (c) after 126 min. The surface height profile of (c) shows the *A*-direction projected on the given sample cross-section. This shows why ripples break the sample surface (at e.g., arrow X). (d–f) Sample SF5; width of images is 3 μm: (d) after 3 min; (e) after 14 min; (f) after 57 min. (g–i) Sample S3; stress is 46 MPa in the *B*-direction; width of images is 2.5 μm; (g) after 11 min; (h) after 22 min; (i) after 107 min.

not affect the dissolution behaviour much in miscut samples. The dissolution pattern in Fig. 6c is not formed by sharp dissolution steps bordering flat terraces, but appears more as consisting of fine ripples with rounded convex shapes. The average ripple-width in Fig. 6c is larger than the average step spacing in Fig. 6b, 50 nm vs. 30 nm, respectively (Fig. 7a). This pattern coarsening could have been a result of progressive coalescence of elementary dissolution steps. The ripples have to break the surface (at the arrow X in Fig. 6c, for example), since the *A*-direction does not lie in the plane of the sample surface in the case of miscut samples.

As in sample SF3, initial dissolution in SF5 occurred along steps in the *A*-direction. The surface coarsened in time, possibly due to a step-bunching process leading to

larger step height and terrace width (Figs. 6d–f and 7a). During coarsening the distribution of step-spacings broadened (Fig. 8a). In comparison to the sharp pattern of retreating dissolution steps in Fig. 3f, the step-pattern in Fig. 6f is more rounded, i.e., terraces gradually curve into steps. In addition to steps along the *A*-direction, sample SF3 showed the appearance of distinct mound-like features dispersed over the stepped surface (arrow I in Fig. 6f). Similar features in a possibly less advanced state are also indicated with arrows in Fig. 6f. Due to the relatively strong tip-effect on pattern formation we were not be able to monitor the development of a single mound feature. However, on close inspections of Figs. 6d and e similar mound-like features on a much smaller scale can be observed and it appears that these mounds are scaled with the step-spacing in
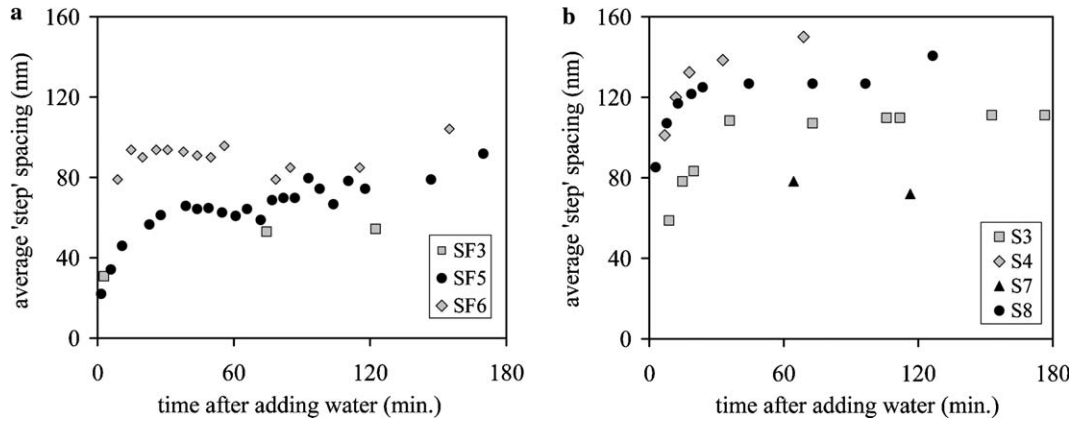
Fig. 7. Pattern-coarsening in stress-free (a) and stressed (b) calcite samples with a 5° miscut. The average step-spacing or ripple-width is measured along three transects perpendicular to the *A*-direction. All feature edges crossing transects perpendicular to the *A*-direction were counted. Standard deviations for a number of data points are given in Fig. 8.
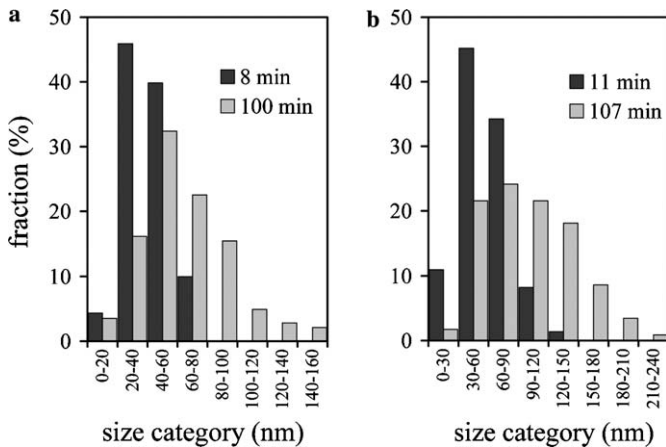

Fig. 8. Evolution of step-spacing distribution in sample SF5 (a) and ripple-width distribution in sample S3 (b). Note the different category scales in (a) and (b).

size. For this reason we believe that these mounds became larger by growth, i.e., local addition of material to the surface, and not by local delayed dissolution of the surface.

Pattern formation in stressed samples was in general similar to stress-free samples. In 4 of the 6 stressed samples initial dissolution steps changed into convex ripples with an *A*-direction (e.g., Figs. 6g–i). The average step-spacing or ripple-width increased mainly in the first 30–40 min of the experiments (Fig. 7b). During coarsening the distribution of ripple widths broadened (Fig. 8b). As in stress-free samples, variation existed in the shape of steps or ripples. In some cases ripples had long straight edges as in Fig. 6c, in others ripples were overgrown by dispersed mound-like features as in Fig. 6e. In sample S3 some of the ripples appear to be complete formed by an alignment of these mound features (Fig. 6i). The average size of distinct mounds (examples indicated with arrows) appears to increase in size, contemporary with the increase in ripple width (Figs. 6g–i). This indicates that mound features are not 'left-overs' due to local delayed dissolution, but are due to addition of material to the surface. Ripple-coarsening

and appearance of mound-like features in stress-free and stressed samples led, on average, to a minor increase in surface area (Fig. 9). No relationship was found between the shape of steps or ripples and the Mn, Sr, or Mg contents of the source crystals (Table 1).

In samples SF6, S4, and S8, initially no long dissolution steps in the *A*-direction developed as in the other samples. Instead, at the start of experiments the sample surfaces were coated with many round mound-like features with a size of about 100 nm (Fig. 10). This initial coating had a significant affect on subsequent pattern evolutions as these samples showed the coarsest patterns (Fig. 7) and a much larger increase in surface area compared to the 'non-coated' samples (Fig. 9). Only in later stages of these experiments ripple-like features in the *A*-direction formed (Fig. 10c). In the stressed samples (both with and without initial coating) dissolution led on average to coarser patterns than in stress-free samples (Fig. 7).

Sample S3 and to a lesser extent sample S4 showed formation of long and straight ridges on the micrometer scale, some standing as high as 50 nm out of the surface (Fig. 11a). Occasionally, similar but smaller ridges were observed in other stressed and some stress-free samples (e.g., Fig. 11b). The ridges in S3 and S4 formed a pattern similar to patterns formed by larger cross-cutting polishing scratches sometimes observed on the dry starting surface. These ridges probably were a result of enhanced growth adjacent to polishing scratches since they were formed by an alignment of mound growth features (Fig. 11b).

4. Discussion

4.1. Dissolution rate in semi-stagnant water

In the AFM-experiments the deionized water in the fluid cell was refreshed in between taking images, every 5 or 10 min. Apart from fluid movement caused by the scanning AFM tip the conditions of the fluid during image acquisition was therefore stagnant. On the hour time scale of a
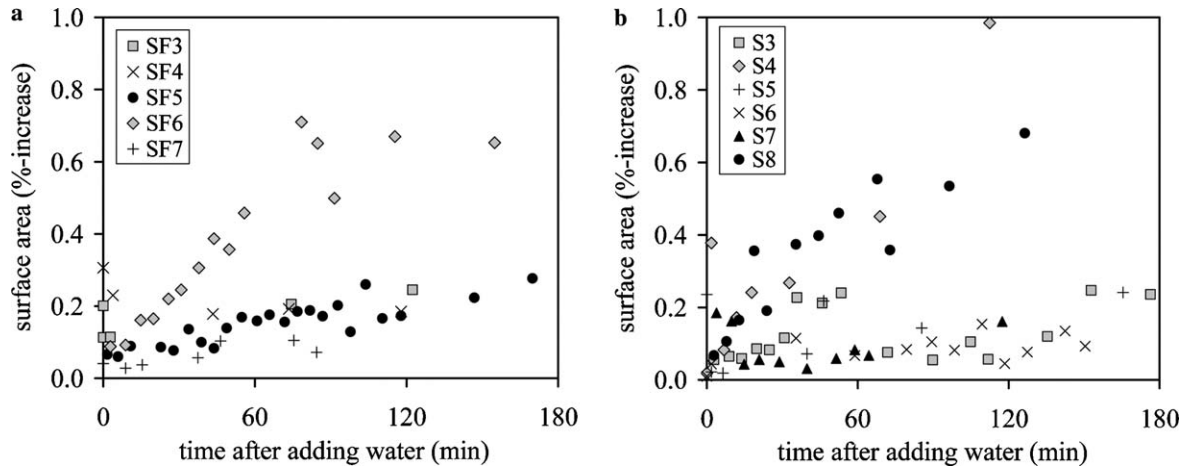
Fig. 9. Surface area development of stress-free (a) and stressed (b) calcite samples with a 5° miscut. Surface area is given as: $(A_{3D}/A_{2D} - 1) \times 100\%$. Measurements from AFM height-images of 3×3 μm or 5×5 μm after second order flattening of the images. Surface areas of sample S3 measured in between the large precipitation ridges (Fig. 11).
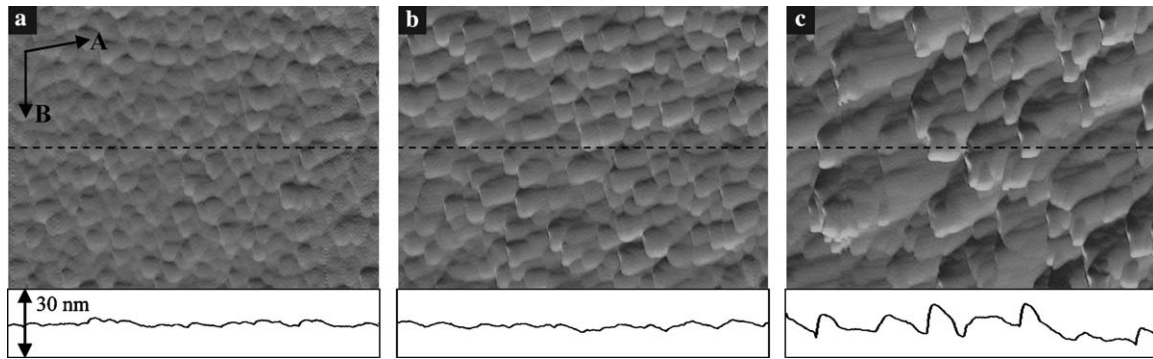

Fig. 10. In situ AFM (deflection) images of sample S4, one of the three samples that were completely coated with small mound-like features soon after adding the water. Images taken at different locations. The height profile curves are given for the dashed line in the AFM images. Height axis is 30 nm in all these images; stress is 46 MPa in the *B*-direction; width of images is 2.5 μm (a) after 9 min; (b) after 14 min; (c) after 71 min.
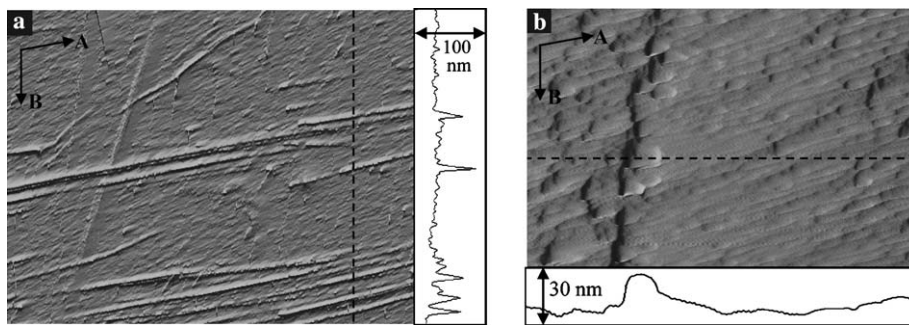

Fig. 11. In situ AFM (deflection) images of growth-ridges interpreted to have formed next to polishing scratches. (a) Sample S3 after 133 min; stress is 46 MPa in the *B*-direction; image width is 70 μm. (b) Sample SF5 after 74 min; image width is 3 μm.

single experiment we refer to the fluid condition as semi-stagnant. Under such semi-stagnant fluid conditions the calcite dissolution rate was probably continuously fluctuating on a time scale of 5 or 10 min. The magnitude of short-term fluctuations in dissolution rate will depend on whether dissolution is reaction or transport rate limited in the periods that the fluid is stagnant and this can depend on the reactivity of the calcite surface.

Samples that were polished parallel to $\{10\bar{1}4\}$ cleavage planes initially had a low density of elementary steps and dissolution originated from polishing defects. The formation of etch-pits in these samples indicates that the fluid in contact with the surface initially remained significantly undersaturated. A shown by Teng (2004) a saturation index Ω below 0.541 is required to nucleate (and deepen) dislocation etch-pits on the calcite cleavage surface. Widening
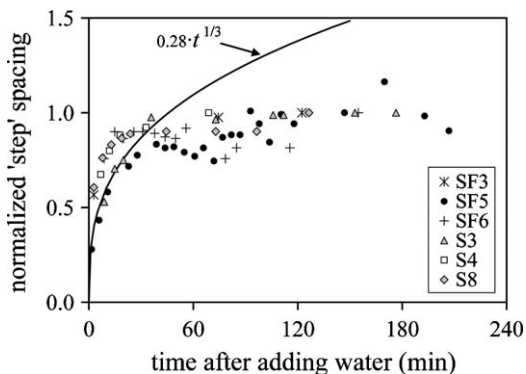
Fig. 12. Normalized pattern coarsening in stressed and stress-free samples plotted in Fig. 7. Data points are normalized with respect to the maximum average step/ripple width measured in each experiment (see text for discussion).

and deepening of etch-pits led to the creation of longer and new steps, respectively, and thus to an increased flux of atoms leaving the surface. As a result the saturation index of the fluid just above the calcite surface is expected to have gradually increased and the dissolution became more and more transport limited. This explains why no new etch-pits are nucleated later in the experiments and why the existing ones developed flat bottoms (Figs. 3a–c). The gradual increasing saturation index of the near-surface fluid is also indicated by the progressive rounding of the corner formed by the obtuse etch-pit walls (Figs. 3a–c). Lea et al. (2001) showed that the degree of rounding of this corner increased with $[CO_3^{2-}]$ concentration in the aqueous solution.

In samples polished with a 5° miscut to cleavage planes, it is likely that dissolution was already transport-limited at the start of the experiments due to the high flux of atoms that could potentially have left the surface. With an elementary step-height in calcite of 3.3 Å (De Giudici, 2002) a 5° miscut surface has 258 elementary steps per μm^2. If we assume that for our miscut direction acute steps were active and that these steps can attain a step-retreat rate of 1.25 nm/s (Liang and Baer, 1997; De Giudici, 2002). Then, with a molar volume of calcite of 36.94 cm^3, the dissolution rate of the 5° miscut surface would be 2.9×10^{-7} mmol cm^{-2} s^{-1} if the dissolution is reaction rate limited. This potential maximum dissolution rate corresponds well with the dissolution rate of 1.9×10^{-7} mmol cm^{-2} s^{-1} measured for a 5° miscut surface in a stirred 0.3 M aqueous KCl solution (Compton et al., 1986). We assume that in stagnant deionized water such high surface reaction rate can not be maintained and that the dissolution rapidly becomes transport rate limited. The fluid-layer of 3–4 mm on top of the sample will probably make the dissolution limited by diffusion of CO_2 or H^+ to the calcite surface (Buhmann and Dreybrodt, 1985). The miscut surface is expected to always have had the potential reactivity to consume the protons supplied to the reaction surface such that the saturation index of

the near-surface fluid remained high. That calcite dissolution rapidly becomes diffusion limited in a stagnant fluid is also shown by the significant decrease in step retreat rate measured with AFM under such conditions (Liang and Baer, 1997).

4.2. Pattern coarsening in miscut samples

Dissolution of miscut samples led to stepped or rippled patterns that coarsened until an apparent steady-state pattern was reached after about 30–40 min into the experiments (Fig. 12). Two possible reasons for the pattern coarsening are: (i) progressive bunching of retreating dissolution steps or (ii) surface recrystallization driven by miscut surface energy or elastic strain energy. From the cleavage-parallel samples it is evident that elementary steps may bunch during dissolution when their spacing is small (Fig. 3). Fig. 3f shows the formation of steep macrosteps due to step-bunching in former etch-pit walls, while many elementary steps unrelated to etch-pits had much larger spacings and did not bunch. In samples with a 5° miscut, the spacing between elementary steps is relatively small (as in etch-pit walls) and therefore they may bunch during dissolution. Progressive coalescence of retreating steps would lead to a macro-stepped or rippled dissolution pattern.

Additionally, surface recrystallization could be an explanation for the observed pattern coarsening. Miscut samples showed, to varying degrees, the growth of mound-like features. These mounds grew in size contemporary with the increase in step or ripple width, but they are hard to explain as being formed by a process involving retreating dissolution steps only. Therefore, we believe that the mounds are formed by local addition of material to the surface. Dissolution of miscut samples was likely to be transport limited and for this reason the fluid just above the miscut surface is expected to have attained a high saturation index (see Section 4.1.). Under such conditions, surface energy of a miscut surface or elastic strain energy could have driven recrystallization of the surface by a dissolution–precipitation process. Simultaneous dissolution and growth of calcite in a near but undersaturated fluid has previously been observed in AFM experiments by Dove and Hochella (1993). A good indication that growth mounds were a result of surface recrystallization and not a result of precipitation upon potential temperature fluctuations in the fluid, is the observations of growth-ridges next to polishing scratches (Fig. 11). Larger polishing scratches probably had a higher local surface or elastic strain energy than the 'unscratched' sample surface and therefore showed a higher degree of growth in their proximity.

Growth mound features were observed in both stress-free and stressed samples and therefore elastic strain energy was not the main driving force for the observed surface recrystallization. Nonhydrostatic thermodynamics predicts a small effect of surface-parallel stress on the solubility of

calcite. For instance, a surface parallel stress of 45 MPa (Table 2) would only increase the solubility of calcite by a factor of 1.0003 relative to stress-free calcite (see Appendix A). This could also explain why applied elastic strain did not have a measurable effect on the rate of etch-pit formation in cleavage-parallel samples (Fig. 5). The stressed miscut samples showed on average coarser patterns (Fig. 7). However, in samples S4 and S8 it could have been their initial 'coating' (Fig. 10) and not stress that led to their relatively high pattern coarseness later in these experiments. Elastic strain energy associated with dislocations also has a relatively small effect on calcite solubility (Schott et al., 1989) and therefore dislocations introduced by polishing are not expected to have been an important driving force of recrystallization of miscut surfaces. As mentioned in the introduction, a competition between elastic strain energy and surface energy under near-equilibrium conditions may lead to a surface morphology with a characteristic wavelength. This characteristic wavelength (λ_c) can be estimated by a linear stability analysis of this stress-induced surface instability (see Appendix A). For calcite, with $\gamma = 94 \text{ mJ m}^{-2}$ (Stumm, 1992), $E = \sim 57 \text{ GPa}$ in the [0$\bar{4}$41]-direction, and a stress of 45 MPa (Table 2), λ_c would be of the order of 20 μm. The characteristic wavelength of surface patterns λ (ripple width) in this study is on a much smaller scale (~ 0.1 μm), both in stressed and stress-free samples, and therefore not stress-related.

Pattern-coarsening and growth of mound features could have been driven by a minimization of surface energy. A miscut surface with many elementary steps has a higher surface energy than a singular crystal face (e.g., Venables, 2000) and therefore may recrystallize in a saturated solution. Surface energy driven recrystallization of particles in a saturated solution, i.e., Ostwald ripening, leads to coarsening of particles (Chai, 1974; Morse and Casey, 1988): Small particles with the highest surface curvature dissolve and re-precipitate as larger particles with a lower surface energy. Similarly, small ripples on a miscut surface may ripen into larger ripples or mounds to minimize surface energy. Ripening of 'miscut' crystal surfaces (i.e., surfaces not appearing on the equilibrium crystal shape) is well know in metallurgy as *thermal faceting*. Upon heating, such energetically unfavorable surfaces may break up into a hill-and-valley structure so as to lower its total surface free energy in spite of a larger surface area (Liu and Metiu, 1993). The evolution from a flat polished miscut surface to a rippled surface as observed in the miscut calcite samples could be a phenomenon similar to thermal faceting. Like Ostwald ripening of particles, the typical wavelength (λ) of the hill-and-valley structure is predicted to coarsen according to $\lambda \sim t^{1/3}$ when material transport occurs by volume diffusion (Flytzani-Stephanopoulos and Schmidt, 1979).

In Fig. 11 the normalized pattern coarsening of all samples given in Fig. 7 has been plotted. It is evident that an Ostwald ripening coarsening curve ($\lambda \sim t^{1/3}$) cannot be fitted to the global coarsening behaviour of the samples.

Up to 40 min a $\lambda \sim t^{1/3}$ coarsening curve can be fitted to the data of experiments SF5 and S3 (the other samples better fit a $\lambda \sim t^{1/4}$ coarsening curve in the first 40 min), but subsequently coarsening slowed down rapidly or stopped. An explanation could be that ripening of slowly dissolving miscut surfaces (under transport limited dissolution conditions) does not continue endlessly. More experiments are required, under a range of fluid conditions and miscut angles, to elucidate the importance of step-bunching and Ostwald ripening during dissolution of calcite miscut surfaces.

5. Conclusions

Polished calcite surfaces are suitable for AFM studies and enable to study the effect of crystallographic orientation and surface stress on calcite dissolution and precipitation processes. Defects caused by sample preparation did not have an observable effect on the dissolution behaviour of surfaces polished with significant ($>5°$) miscut to cleavage planes (i.e., no etch-pits formed on these surfaces).

Dissolution of 5° miscut samples led to stepped or rippled surface patterns that coarsened until an apparent steady-state pattern was reached after about 30–40 min into the experiments. Possible reasons for the pattern-coarsening were: (i) progressive bunching of retreating dissolution steps and (ii) surface energy driven recrystallization under transport limited dissolution conditions. Similar to the phenomena known as *thermal faceting* in metallurgy, a flat polished miscut surface in calcite may break up into a nanoscale hill-and-valley structure in a (near-)saturated solution so as to lower its total surface free energy in spite of a larger surface area.

No clear effect of applied elastic strain on pattern formation in both cleavage parallel and miscut samples was observed. Elastic strain energy probably was a relatively small driving force compared to other driving forces (surface energy and undersaturated fluid) of pattern formation in our experiments. The absence of etch-pit formation on miscut surfaces implies that plastic deformation (dislocation density) does not have a significant effect on calcite dissolution in nature, since calcite surfaces like grain boundary and fracture surfaces are expected to be miscut surfaces in general.

manuscript was substantially improved by the comments made by three anonymous reviewers and the Associate Editor.

Associate editor: William H. Casey

Appendix A

The thermodynamic relationship between surface-parallel stress and the solubility of a solid in a fluid is given by (Paterson, 1973)

$$a_s c_s = a_0 c_0 \exp V_0 \sigma^2 / 2ERT,$$

where a_0, a_s, and c_0, c_s are activity coefficients and concentrations, respectively, of the solid in the solution at local equilibrium with a stress-free (a_0, c_0) and a stressed (a_s, c_s) dissolution front. V_0 is the molar volume (36.94 cm^3 mol^{-1}), σ is differential stress in the solid, E is the Young's modulus (≈ 57 GPa in the $[0\bar{4}41]$-direction), T is temperature (298 K) and R is the universal gas constant (8.314 kg m^2 mol^{-1} K^{-1} s^{-2}). For a surface stress (σ) of 45 MPa (Table 2) $a_s c_s / a_0 c_0 = 1.0003$.

A.1. Grinfeld instability

According to Srolovitz (1989) the change in free energy (ΔF) in going from a flat stressed surface (of an isotropic solid) to a stressed surface consisting of valley and ridges with an amplitude c and a wavelength λ may be approximated by

$$\Delta F = (-c\lambda \sigma^2)/4E + 2c\gamma,$$

where σ is the differential stress in the bulk, γ is the surface energy, and E is the Young's modulus. This equation shows that the formation of a 'rough' surface profile lowers the energy of the system provided that the roughness wavelength of the surface is above a critical wavelength (i.e., the wavelength at $\Delta F = 0$)

$$\lambda_c = (8\gamma E)/\sigma^2.$$

For calcite, with $\gamma = 94$ mJ m^{-2} (Stumm, 1992), $E = \sim 57$ GPa in the $[0\bar{4}41]$-direction, and a stress of 45 MPa (Table 2), λ_c would be of the order of 20 μm. In isotropic solids, surface perturbations with a wavelength smaller than λ_c would decay because the surface energy dominates over the elastic strain energy.

References

Buhmann, D., Dreybrodt, W., 1985. The kinetics of calcite dissolution and precipitation in geologically relevant situations of karst areas: 1. Open system. *Chem. Geol.* **48**, 189–211.

Chai, B.H.T., 1974. Mass transfer of calcite during hydrothermal recrystallization. In: Hofmann, A.W. et al. (Eds.), *Geochemical Transport and Kinetics*. Carnegie Inst., Washington, pp. 205–218.

Compton, R.G., Daly, P.J., House, W.A., 1986. The dissolution of Iceland Spar Crystals: The effect of surface morphology. *J. Colloid Interface Sci.* **113**, 12–20.

De Bresser, J.H.P., 1996. Steady state dislocation densities in experimentally deformed calcite materials: single crystals versus polycrystals. *J. Geophys. Res.* **101** (B10), 22189–22201.

De Bresser, J.H.P., Spiers, C.J., 1997. Strength characteristics of the r, f, and c slip systems in calcite. *Tectonophysics* **272**, 1–23.

Den Brok, S.W.J., Morel, J., 2001. The effect of elastic strain on the microstructure of free surfaces of stressed minerals in contact with an aqueous solution. *Geophys. Res. Lett.* **28**, 603–606.

De Giudici, G., 2002. Surface control vs. diffusion control during calcite dissolution: dependence of step-edge velocity upon solution pH. *Am. Mineral.* **87**, 1279–1285.

Dove, P.M., Hochella Jr., M.F, 1993. Calcite precipitation mechanisms and inhibition by orthophosphate: in situ observations by Scanning Force Microscopy. *Geochim. Cosmochim. Acta* **56**, 705–714.

Engelder, T., 1982. A natural example of the simultaneous operation of free-face dissolution and pressure solution. *Geochim. Cosmochim. Acta* **46**, 69–74.

Flytzani-Stephanopoulos, M., Schmidt, L.D., 1979. Morphology and etching processes on macroscopic metal catalysts. *Prog. Surface Sci.* **9**, 83–111.

Gutman, E.M., 1994. *Mechanochemistry of Solid Surfaces*. World Scientific, Singapore, pp. 39–43.

Koehn, D., Dysthe, D.K., Jamtveit, B., 2004. Transient dissolution patterns on stressed crystal surfaces. *Geochim. Cosmochim. Acta* **68**, 3317–3325.

Liang, Y., Baer, D.R., 1997. Anisotropic dissolution at the CaCO$_3${10$\bar{1}$4}-water interface. *Surface Sci.* **373**, 275–287.

Liu, F., Metiu, H., 1993. Dynamics of phase separation of crystal surfaces. *Phys. Rev. B* **48** (9), 5808–5817.

Lea, A.S., Amonette, J.E., Baer, D.R., Liang, Y., Colton, N.G., 2001. Microscopic effects of carbonate, manganese, and strontium ion on calcite dissolution. *Geochim. Cosmochim. Acta* **65**, 369–379.

MacInnis, I.N., Brantley, S.L., 1992. The role of dislocations and surface morphology in calcite dissolution. *Geochim. Cosmochim. Acta* **56**, 1113–1126.

Misbah, C., Renard, F., Gratier, J.P., Kassner, K., 2004. Dynamics of a dissolution front for solids under stress. *Geophys. Res. Lett.* **31**, L06618. doi:10.1029/2003GL019136.

Morel, J., Den Brok, S.W.J., 2001. Increase in dissolution rate of sodium chlorate induced by elastic strain. *J. Cryst. Growth* **222**, 637–644.

Morse, J.W., Casey, W.H., 1988. Ostwald processes and mineral paragenesis in sediments. *Am. J. Sci.* **288**, 537–560.

Paterson, M.S., 1973. Nonhydrostatic thermodynamics and its geological applications. *Rev. Geophys. Sp. Phys* **11** (2), 355–389.

Schott, J., Brantley, S., Crerar, D., Guy, C., Borcsik, M., Willaime, C., 1989. Dissolution kinetics of strained calcite. *Geochim. Cosmochim. Acta* **53**, 373–382.

Spiers, C.J., De Meer, S., Niemeijer, A.R., Zhang, X., 2004. Kinetics of rock deformation by pressure solution and the role of thin aqueous films. In: Nakashima et al. (Eds.), *Physicochemistry of Thin Film Water*. Universal Academy Press Inc., Tokyo, Japan, pp. 129–158.

Srolovitz, D.J., 1989. On the stability of surfaces of stressed solids. *Acta Metall.* **37** (2), 621–625.

Stumm, W., 1992. *Chemistry of the Solid Water Interface*. Wiley, New York.

Teng, H.H., 2004. Controls by saturation state on etch pit formation during calcite dissolution. *Geochim. Cosmochim. Acta* **68**, 253–262.

Venables, J.A., 2000. *Introduction to Surface and Thin Film Processes*. Cambridge University Press, Cambridge, p. 6.

Watts, A.B., 2001. *Isostasy and Flexure of the Lithosphere*. Cambridge University Press, Cambridge, pp. 91–92.